Springer

KSME

Journal of Mechanical Science and Technology 30 (8) (2016) 3729~3739
www.springerlink.com/content/1738-494x(Print)/1976-3824(Online)
DOI 10.1007/s12206-016-0735-z

Numerical investigation of the effects of geometric parameters on transverse motion with slanted-groove micro-mixers †

Seung Joo Baik, Jae Yong Cho, Se Bin Choi and Joon Sang Lee*

School of Mechanical Engineering, Yonsei University, Seoul 120-749, Korea

(Manuscript Received July 1, 2015; Revised January 30, 2016; Accepted April 26, 2016)

Abstract

We investigated hydrodynamic phenomena inside several passive microfluidic mixers using a Lattice Boltzmann method (LBM) based on particle mesoscopic kinetic equations. Mixing processes were simulated in a Slanted grooved micro-mixer (SGM), a Staggered herringbone grooved micro-mixer (SHM), and a Bi-layered staggered herringbone grooved micro-mixer (BSHM). Then, the effects of six geometric mixer parameters (i.e., groove height to channel height ratio, groove width to groove pitch length ratio, groove pitch to groove height ratio, groove intersection angle, herringbone groove asymmetric ratio and bi-layered groove asymmetric ratio) on mixing were investigated using computed cross-flow velocity and helicity density distributions in the flow cross-section. We demonstrated that helicity density provides sufficient information to analyze micro helical motion within a micro-mixer, allowing for micro-mixer design optimization.

Keywords: Cell sorting; Passive microfluidic mixers; Staggered herringbone grooved micro-mixer; Lattice Boltzmann method; Helicity

1. Introduction

Certain rare cells in humans, such as Circulating tumor cells (CTCs), provide critical information about diseases [1-3]. However, these rare cells are difficult to sort due to their low concentration (1 CTC per 109 blood cells) [3, 4]. Efficient cell separation techniques are therefore essential to obtain highly purified populations of cells for diagnostic and biomedical applications. Cell sorting techniques have progressed largely through the development of lab-on-a-chip devices based on microfluidic systems [5-9]. Multiple batch separation technologies have also been employed to capture targeted cells [9]. One cell sorting technique, cell affinity chromatography, captures targeted cells from a heterogeneous cell population through selective binding to high-affinity ligands immobilized on a substrate [10, 11]. In cell affinity chromatography, mixing within micro-channels disrupts streamlines and enhances collisions between target cells and substrates, resulting in improved ability to sort targeted cells from the fluidic specimen [12].

However, mixing of fluids in microsystems remains a challenge due to the inherent limitations of small channel dimensions and the limited range of achievable flow rates. The Reynolds number, $Re = \rho vD/\mu$ where D is the most relevant length scale, ρ is the density of the fluid, v is the average velocity of the fluid flow, and μ is the dynamic viscosity of fluid, can be used to determine whether the flow is laminar or turbulent. Because of the micro-scale dimensions, the Reynolds number in microsystems is generally less than 100. Under these conditions, flow inside a planar micro-channel is fully laminar, and uniaxial flow conditions usually dominate. Therefore, cells follow streamlines and display minimal diffusion across channels. This limited interaction between cells and substrates under laminar flow conditions results in sluggish cell separation.

Numerous micro- mixing devices have been developed, including active and passive mixing types [13]. External energy sources such as hydrodynamic pressure [14], electro-hydrodynamic forces [15], magneto-hydrodynamic forces [16], ultrasound, and acoustic vibrations [17, 18] have been used to create a stirring effect in active mixing processes. Integration of external energy sources in a micro-mixer usually requires complicated fabrication processes. In contrast, passive mixers are much easier to integrate into microsystems as passive mixing relies on diffusion or chaotic advection and does not require complicated fabrication processes. Chaotic advection can be generated by designing micro-channels with specific geometrical structures. Proper geometric design is the most important factor for chaotic advection because of its dependence on geometry. Micro-pillars [11], curved-channels [19, 20], converging-diverging channels [21], 3D serpentine chan-

*Corresponding author. Tel.: +82 2 2123 5820
E-mail address: joonlee@yonsei.ac.kr
† Recommended by Associate Editor Jaeseon Lee

nels [22], and other designs have been developed to enhance mixing efficiency.

Because passive micro-mixer performance depends on geometry, numerical simulations are used for analysis of these systems. However, numerical simulations have drawbacks associated with computation time and memory [23]. Ideally, we must find a method of obtaining appropriate complex geometry and determining the mixing efficiency with the use of numerical simulations.

A staggered herringbone-grooved pattern is a representative geometry among many possible geometries. Stroock et al. used bas-relief patterned structures as channel structures and referred to the resulting mixer as a Staggered herringbone mixer (SHM) [24]. This micro-mixer was constructed with slanted ridges to induce a steady axial pressure gradient, which generated transverse flows in the channel. Efficient mixing was achieved because of the helical flow patterns induced by the bas-relief structures. Stroock et al. experimentally determined the magnitude of the transverse flow using optical microscopy and compared these experimental results to analytical results [24]. Hardt et al. presented a helical flow simulation for an SHM using transverse velocity analysis based on a solution to the incompressible Navier-Stokes equation and a convection-diffusion equation [25]. Li et al. investigated the optimized groove width fraction and groove number for a half cycle using a lattice Boltzmann numerical model [26]. Dandy et al. reported that mixing in an SHM is highly dependent on channel aspect ratio, groove depth ratio and ridge length [27]. Based on an analysis of streamlines in a SHM, Kralj et al. proposed that the groove depth and groove width in the channels of an SHM had significant effects on particle-surface interaction [28].

In order to evaluate the mixing index, various hydrodynamic properties of the fluid have been studied in micro-mixers. Wang et al. measured the mean value of helicity which relies on groove aspect ratio, width of the grooves and depth of channel in micro-mixer and, especially, high aspect ratio contributed to the high helicity which improve the mixing performance [29, 30]. Mastrangelo et al. found that helicity dencity is promising in proper vortices detection at low Reynolds number: A curved microchannel geometry served to test vortex identification methods and micing performance [31]. Geyer et al. employed the helicity to quantify and visualize Dean vortex cores in flow which promote fluid mixing transverse to the main flow direction [32].

In this study, we designed passive mixing systems with a low Reynolds number (near 1) and simulated flow to optimize mixing performance. We analyzed transverse flow patterns and structures of vortices in fluid flow in a Slanted-groove mixer (SGM), a Staggered-herringbone grooved mixer (SHM), and a Bi-layered staggered-herringbone grooved mixer (BSHM) using the D3Q19 incompressible lattice Boltzmann numerical model. To optimize the performance of the passive mixing channels, several geometric variations were examined including the groove-channel height ratio, the aspect ratio of the channel, the groove width-pitch ratio, the groove pitch to groove height ratio, the angle between the channel and the groove, and the width fraction of the groove in the channel. We also analyzed the hydrodynamic properties of the fluid flow inside the micro-channel, namely cross-flow velocity, helicity density distribution and velocity fluctuation of the fluid. Overall contents and objectives of this paper are shown in Fig. 1.

Table 1. Numerical values of geometric parameters.

Design parameters	α	κ	δ	θ (deg)	η	γ
Variation range	0.2 0.4 0.6 0.8 1.0 1.2 1.4 1.6	0.125 0.250 0.375 0.500 0.625 0.750 0.875	1.0 1.5 2.0 2.5 3.0 3.5 4.0	30 35 40 45 50 55 60	0.5 0.55 0.60 0.65 0.7 0.75 0.8	0.125 0.250 0.375 0.500

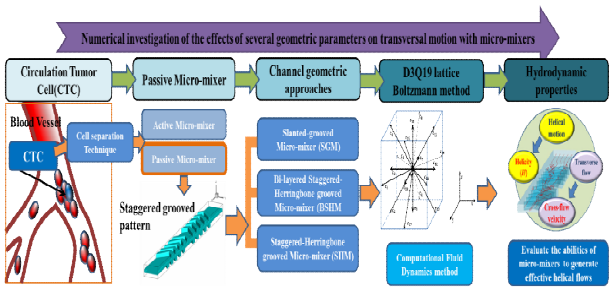

Fig. 1. Schematic diagram summarizing this study.

2. Geometric design standard

Micro-channels had a planar rectangular section duct geometry. The slanted-herringbone geometry we used is shown in Fig. 2. Uniform streamwise velocity occurs at the channel inlet. The initial channel dimensions chosen for simulations were a channel width (w_{ch}) of 300 μm and a channel height (h_g) of 50 μm. To study the hydrodynamics of flow inside the micro-mixers, we choose three basic types of micro-mixers, as shown in Fig. 3. We simulated flow for the three geometric designs of a SGM [24], a SHM [24] and a BSHM [33, 34]. We assigned five geometric parameters to the micro-mixer design. We initially chose three geometric parameters for the SGM case shown in Fig. 3(a) including groove height (h_g) to channel height (h_{ch}) ratio ($\alpha = h_g/h_{ch}$), groove intersection angle (θ), groove width (l_g) to groove pitch length (l_p) ratio ($\kappa = l_g/l_p$), and groove pitch to groove height ratio ($\delta = l_p/h_g$). Due to its simple geometric design, the SGM case was utilized to study the effects of geometry on the magnitude of the transverse and helical flows. The magnitude of helical flow within an SGM is closely related to those within an SHM and BSHM [27]. We chose the herringbone groove asymmetric ratio (η =

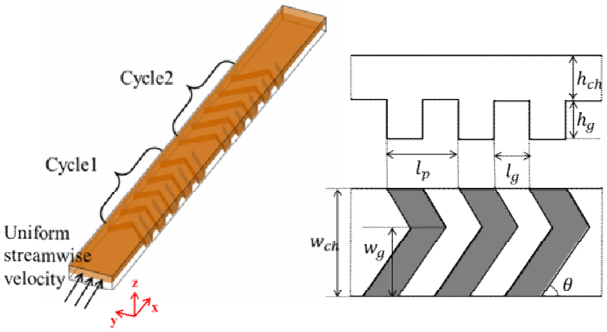

Fig. 2. Parameters in slanted grooved micro-mixer in this study.

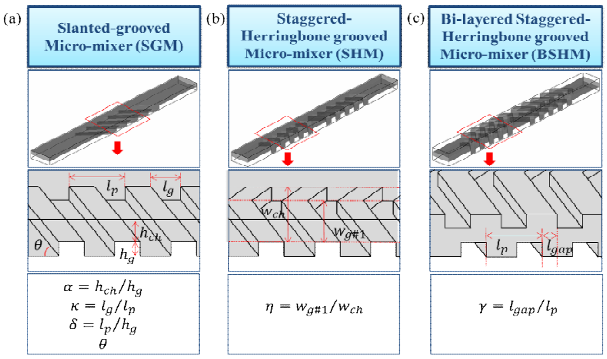

Fig. 3. Selection of geometric parameters for (a) a Slanted-grooved micro-mixer (SGM); (b) a Staggered-herringbone grooved micro-mixer (SHM); (c) a Bi-layered staggered-herringbone grooved micro-mixer.

w_g/w_{ch}) as a geometric parameter for the SHM case shown in Fig. 3(b). Finally, we added another parameter for the BSHM case shown in Fig. 3(c), the bi-layered groove asymmetric ratio ($\gamma = l_{gap}/l_p$). We then estimated the helical flow in each micro-mixer by varying these geometric parameters.

3. Numerical methods

3.1 Lattice Boltzmann method (LBM)

The numerical model used in this study was the 19-velocity incompressible lattice Bhathagar-Gross-Krook (BGK) Boltzmann model (D3Q19) (Qian at el., 1992) [35] for three-dimen- sional cases. LBM models a fluid as virtual particles, where each particle performs consecutive propagation (streaming step) and collision (collision step) processes over a discrete lattice domain. In contrast, the traditional Computational fluid dynamics (CFD) method requires a solution to the conservation equations for macroscopic properties (Succi, 2001). The isothermal, single-relaxation model is derived from the following Boltzmann kinetic equation:

$$\frac{df}{dt} + \xi \cdot \nabla f = -\frac{1}{\lambda}(f - f^{eq}) \tag{1}$$

where f is the density distribution function, ξ is the local particle velocity, f^{eq} is the equilibrium distribution function, and λ is the physical relaxation time. The following equation is derived from discretization of Eq. (1) using velocity sets confined to a finite number of directions:

$$\frac{df_i}{dt} + \xi_i \cdot \nabla f_i = -\frac{1}{\lambda}(f_i - f_i^{eq}). \tag{2}$$

The right hand side of Eq. (2) is the collision operator, Ω_i. The D3Q19 BGK model has 19 velocity direction vectors, as shown in Fig. 3, with the following end point coordinates:

$$\begin{aligned} &e_0(0,0,0); e_1(-1,-1,0); e_2(-1,0,-1); e_3(-1,0,0); \\ &e_4(-1,0,1); e_5(-1,1,0); e_6(0,-1,-1); e_7(0,-1,0); \\ &e_8(0,-1,1); e_9(0,0,-1); e_{10}(1,1,0); e_{11}(1,0,1); \\ &e_{12}(1,0,0); e_{13}(1,0,-1); e_{14}(1,-1,0); e_{15}(0,1,1); \\ &e_{16}(0,1,0); e_{17}(0,1,-1); e_{18}(0,0,1). \end{aligned} \tag{3}$$

Eq. (1) can be further discretized in lattice space and time, leading to the following equation:

$$f_i(\mathrm{x} + c_i\delta_t, t + \delta_t) - f_i(\mathrm{x}, t) = -\frac{1}{\tau}\left[f_i(\mathrm{x}, t) - f_i^{eq}(\mathrm{x})\right]. \tag{4}$$

The equilibrium distribution function f_i^{eq} is calculated using the following formula:

$$f_i^{eq} = \rho\omega_i[1 + \frac{1}{c_s^{\,2}}\mathrm{e}_i \cdot \mathrm{u} + \frac{1}{2c_s^{\,4}}(\mathrm{e}_i \cdot \mathrm{u})^2 - \frac{1}{2c_s^{\,2}}\mathrm{u} \cdot \mathrm{u}] \tag{5}$$

where $c_i = e_i/\delta$ is the lattice velocity in the i^{th}-direction, $c_s = c/\sqrt{3}$ is the speed of sound, and ω_i are weighting factors for each lattice link.

$$\omega_i \begin{cases} \frac{1}{3}, & i = 0 \\ \frac{1}{18}, & i = 3,7,9,12,16,18 \\ \frac{1}{36}, & i = 1,2,4,5,6,8,10,11,13,14,15,17. \end{cases} \tag{6}$$

The relaxation time, τ, is related to the kinematic viscosity, ν, according to the following formula:

$$\nu = (\tau - \frac{1}{2})c_s^{\,2}\delta_t. \tag{7}$$

Macroscopic velocity (u) and density (ρ) can be calculated from the distribution function as:

$$\rho = \sum_{i=0}^{18} f = \sum_{i=0}^{18} f_i^{eq}, \quad \mathrm{u} = \frac{\sum_{i=0}^{18} c_i f_i}{\rho} = \frac{\sum_{i=0}^{18} c_i f_i^{eq}}{\rho}. \tag{8}$$

3.2 Simulation setup

Micro-channels had a planar rectangular section duct geometry. We used a uniform grid ($\Delta x = \Delta y = 2.5\ \mu$m) for all analyses. Boundary conditions for the channel inlet were v_x = constant (= 0.006 m/s), $v_y = v_z = 0$, where constant velocity inlet conditions have no impact on helical flow. We used an extrapolation outlet condition on the outlet, and a no-slip condition was applied to all surfaces using the bounce-back method [36]. The Reynolds number ($Re = \rho v D_H/\mu$) of the studied fluids was calculated to be 0.514 assuming that the fluids were aqueous solutions with a density $\rho = 1\times 10^{-3} kg/m^3$ and a viscosity $\mu = 1\times 10^{-3} kg/ms$. The hydraulic diameter of the rectangular channel ($D_H = 2w_{ch}h_{ch}/(w_{ch}+h_{ch})$) was calculated to be 85.71 μm.

4. Results

4.1 Factors for analysis

To evaluate passive mixing efficacy, different geometries were compared in terms of helicity and cross-flow velocity. Continuous helical motions of fluid flow caused by the bas-relief structures along the channel floor resulted in stretching and folding of the interface between the fluids. This further resulted in an increase in contact area between the fluid and the transverse flow, which is vertical to the main direction of the flow. Therefore, we needed to determine the type of fluid transport from the bas-relief groove that induces large vertical and small helical motions inside the micro-mixer.

Helicity indicates the degree to which velocity field lines wrap and coil around each other [37, 38]. Calculation of helicity involves topological analysis in relation to the linkage of vortex lines of the flow. Helicity of a fluid flow with volume V can be expressed as follows:

$$H = \int_V \boldsymbol{v}\cdot(\nabla\times\boldsymbol{v})dV. \tag{9}$$

Helicity density per unit volume is given by the inner product of the velocity, $\boldsymbol{v}$, and vorticity, $\boldsymbol{\omega} = \nabla\times\boldsymbol{v}$, as follows:

$$H_d = \boldsymbol{v}\cdot(\nabla\times\boldsymbol{v}). \tag{10}$$

The above equation indicates that, when velocity and vorticity vectors are along the same direction, helicity density has its maximum value. In contrast, when velocity or vorticity are zero or when velocity and vorticity vectors are in orthogonal directions, the helicity density value is zero.

Cross-flow velocity can be used to quantify transverse fluid transport. The following equation can be used to calculate the cross-flow velocity of a cross-section where the x-axis is the main direction of the flow.

$$v_{cr} = \sqrt{u_y^{\,2} + u_z^{\,2}}. \tag{11}$$

Here, u_y is the y-component velocity, and u_z is the z-component velocity.

For a homogeneous fluid and incompressible flow, velocities can be split into a mean part and a fluctuating part. The fluctuating part of the velocity can be used to estimate the mixing efficiency of the flow as follows:

$$u_i' = u_i - \overline{u}_i \tag{12}$$

where u_i is the velocity component, and $\overline{u}_i$ is the mean velocity. We calculated the Root mean square (*RMS*) value to evaluate the turbulent intensity which is considered to be the mixing index.

$$u_{rms} = \sqrt{\frac{\sum_{n=1}^{n=N}(u_i-\overline{u}_i)^2}{N}} = \sqrt{\frac{\sum_{n=1}^{n=N}u_i'^2}{N}}. \tag{13}$$

To evaluate omnidirectional properties, we also determined the RMS of velocity fluctuations, which is half of the sum of each velocity fluctuation:

$$RMS\ of\ velocity\ fluctuations = \frac{u_x' + u_y' + u_z'}{2} \tag{14}$$

where u_x' and u_y', u_z' are the velocity fluctuations of each velocity component. The RMS of velocity fluctuations is very small due to the flow conditions; however, the mixing potency of each channel can be compared with this physical property.

4.2 Validation

We validated our numerical model through comparison with the simulation data of Kralj et al. [28]. For SHM simulations, we used a channel width of 500 μm, a channel height of 50μm, a herringbone groove asymmetric ratio of 0.67 and a groove intersection angle of $45°$. We investigated the surface contact percentages according to groove width and depth, as shown in Fig. 4. We assumed that particle motion followed streamlines. We also reasoned that lift forces on a particle caused by interaction with the wall were negligible because of the low Reynolds number ($Re = \rho v D_H/\mu$) and low particle Reynolds number ($Re_p = Re(2R_p/D_h)^2$, $R_p = 9\ \mu$m) for the considered flows. Our simulation results showed good agreement with the results of Kralj and colleagues [28].

For more exact simulation validation, we tried to determine if our grid size of 2.5 μm was a good choice. Generally, the smaller grid size results more exact simulation. Therefore, we used four grid sizes (10 μm, 5 μm, 2.5 μm and 1.25 μm) during simulation of a slanted-grooved micro-mixer with dimensions of $h_{ch} = 50\ \mu$m, $w_{ch} = 300\ \mu$m, $\alpha = 1.0$, $\theta = 45°$ and $\kappa = 0.500$. The results are shown in Fig. 5, illustrating only a small difference between the results for 2.5 μm and 1.25 μm grid sizes. Considering the simulation time, the 2.5 μm grid size is

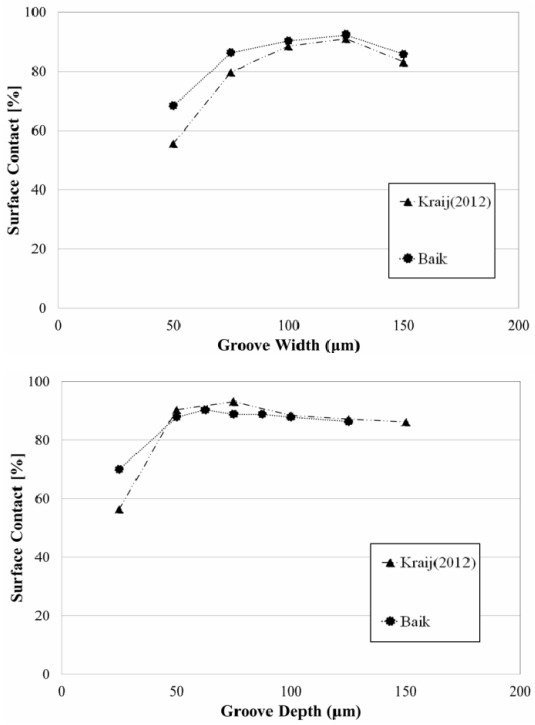

Fig. 4. Comparison of our numerical simulation results with the results of Kralj et al. for channels with different groove widths and depths.

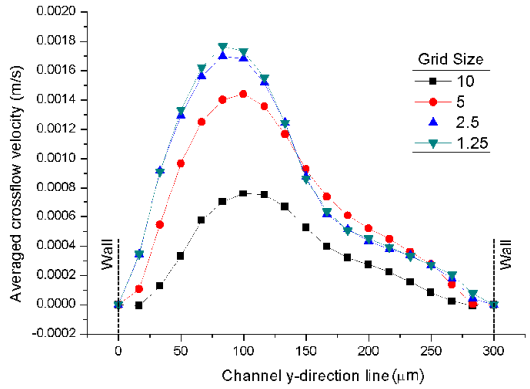

Fig. 5. The grid test for simulation with slanted-grooved micro-mixer.

the best choice for the simulations.

4.3 Slanted-grooved micro-mixers (SGMs)

We next wanted to determine the optimum specific groove design that maximizes helical flow for an SGM. To determine the optimum groove design, fluid flow within several SGMs was calculated for various groove height to channel height ratios (α), groove width to groove pitch length ratios (κ), groove pitch to groove height ratios (δ), and groove intersection angles (θ), as defined in Sec. 2.

First, we investigated the helical flow patterns obtained by varying α from 0.2 to 1.6 with dimensions h_{ch} = 50 μm, w_{ch} = 300 μm, θ = 45° and κ = 0.625. As the oblique grooves were

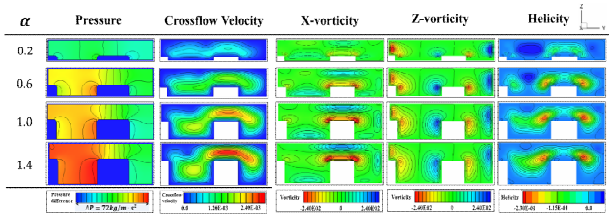

Fig. 6. Pressure contour, cross-flow velocity, x-, z-vorticity and helicity density distribution across the cross-sectional area orthogonal to the mainstream direction for different values of α.

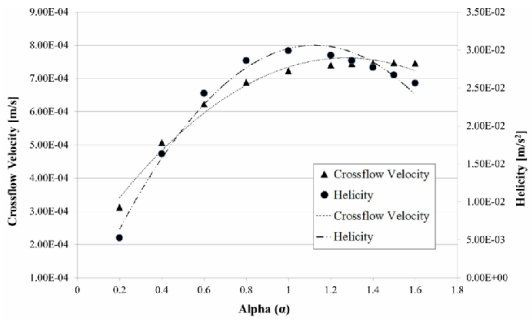

Fig. 7. Mean helicity density and mean cross-flow velocity plots for different values of α. Dotted and dashed lines indicate hyperbolic curve fitting of mean cross-flow velocity and mean helicity density, respectively.

installed above the bottom wall, an streamwise pressure difference was observed. Due to this streamwise pressure difference, a cross-flow velocity was generated and intensified. As the cross-flow velocity was strengthened, *x*-vorticity and *z*-vorticity were also generated and intensified along the protrusion. This indicates that the direction of the vorticity vectors was twisted, contributing to the helical motion within the fluid flow. Helicity density has its highest value at the edge of the protrusion where the *x*- and *z*- vorticity showed their maximum values, as shown in Fig. 6. This demonstrates that the oblique groove and protrusion affect the helical motion of fluid flow.

For low values of α, the flow induced by the groove above the bottom wall did not increase significantly due to the *x*-vorticity, and helicity density only appeared close to the edge of the groove and did not spread over the cross-sectional area of the channel, as shown in Fig. 7. As α increased to 1, the *x*- and *z*-vorticity next to the protrusion increased. In other words, the groove had a significant effect on fluid flow, resulting in increases in cross-flow velocity and helicity density. The mean cross-flow velocity and mean helicity density increased linearly as α increased to 0.8 due to the streamwise pressure difference. Simultaneously, the *x*- and *z*-vorticity along the protrusion increased. The helicity density was six-fold higher at α = 1 than at α = 0.2, and the cross-flow velocity was two times higher.

Meanwhile, when α was larger than 1, the mean cross-flow velocity changed little with changes in α; however, the mean helicity density decreased to 86% of its maximum value. In contrast to the cross-flow velocity distribution within the

grooves, the helicity density was not fully distributed inside the grooves at α = 1.4 due to a decrease in z-vorticity along the protrusion, as shown in Fig. 7. These findings indicate that fluid flow within the lower side of the groove tended to create a large eddy motion, while flow within the upper side of the groove created a small-scale stirring motion.

To further investigate the mixing potency, we calculated the velocity fluctuation and Root-mean-square (*RMS*) value of each velocity component for different values of α. The RMS of velocity fluctuations showed a distribution similar to that of the vertical distribution of RMS values of u_x. (See Figs. 8(a) and 9). It is important to note that the scale of u_x was 10 times higher than those of u_y and u_z. Thus, fluctuations in u_x had a greater influence on the RMS of velocity fluctuations. However, the velocities of diffusion distant from the stream-wise velocity are important for estimating the mixing potency of flow in the micro-mixers. *RMS* values of u_y and u_z were higher in areas of large cross-flow velocity change. *RMS* values of each velocity component increased as α increased. *RMS* values of u_y and u_z increased drastically as α varied from 0.2 to 1, showing a trend similar to that of the cross-flow velocity distribution shown in Figs. 8(b) and (c). *RMS* values of u_z increased as α increased to 1.6, indicating that the increase in groove depth induced significant fluctuations in the *z*-velocity.

We also investigated secondary flow patterns in response to different values of κ. For κ = 0.125, helicity density and cross-flow velocity induced by the bas-relief grooves were weak along the narrow grooves and did not sufficiently spread over the channel. Due to the narrow width of the groove, the streamwise pressure difference was very weak and had limited ability to generate cross-sectional flow motion. Thus, *x*- and *z*-vorticity was not generated within the channel.

As κ increased, the streamwise pressure difference increased, resulting in a stronger cross-flow velocity. As cross-flow velocity increased, *x*- and *z*- vorticity along the protrusion became stronger. This resulted in a higher helicity density. Both physical parameters increased rapidly as κ reached 0.5. The maximum mean helicity density was observed at κ = 0.5, while cross-flow velocity reached a maximum value at κ = 0.75. When κ was greater than 0.625, cross-flow velocity changed less than did the mean helicity density. This signifies that transverse migration of flow inside the channel did not change drastically for κ values higher than 0.625. However, mean helicity density decreased to about 32% of the maximum value as κ increased from 0.5 to 0.875. When κ increased from 0.625 to 0.875, *z*-vorticity along the protrusion decreased, and *x*- and *z*-vorticity were not sufficiently generated for flow inside the grooves. Thus, the helicity density distribution within the groove became weak and spread because the vorticity induced by the protrusion did not affect flow within the groove, as shown in Fig. 10. For κ = 0.875, fluid flow within the groove tended to create a large eddy motion, and small scale helical motion decreased.

Fig. 11 shows that the maximum transverse migration of the flow was obtained when κ was larger than one; however,

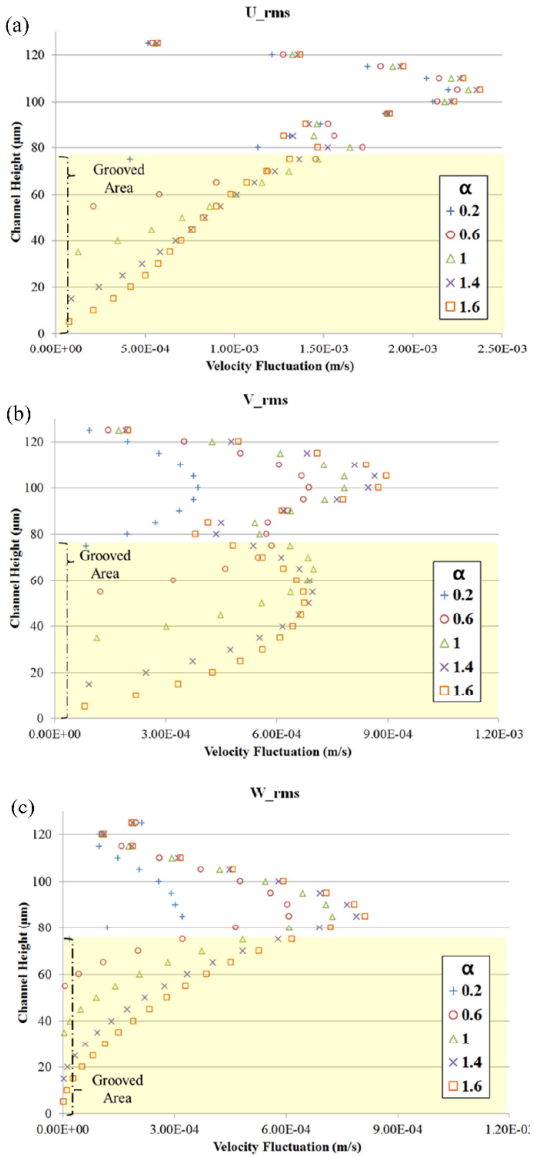

Fig. 8. Vertical profiles of the velocity fluctuation of (a) u_x; (b) u_y; (c) u_z for different values of α.

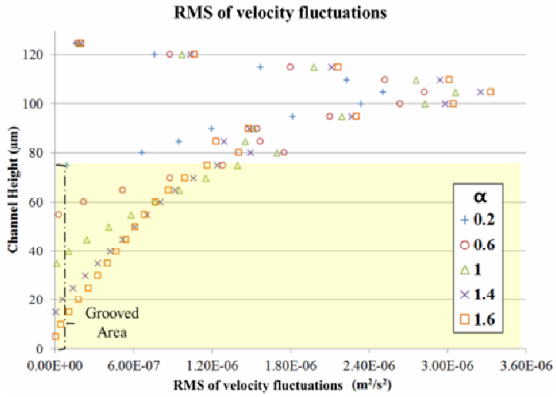

Fig. 9. Vertical profiles of the RMS of velocity fluctuations for different values of α.

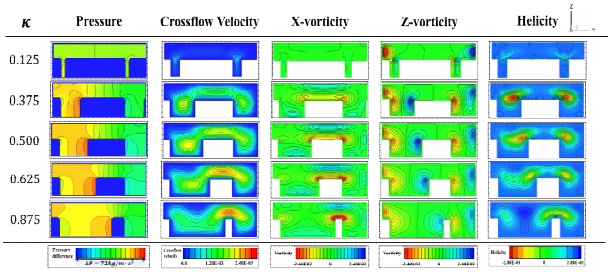

Fig. 10. Pressure contour, cross-flow velocity, x-,z-vorticity and helicity density distribution across the cross-sectional area orthogonal to the mainstream direction for different values of κ.

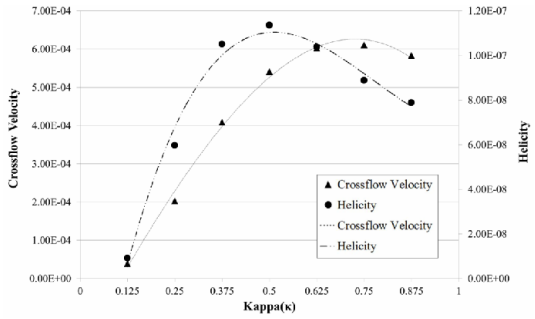

Fig. 11. Mean helicity density and mean cross-flow velocity plots for different values of κ. Dotted and dashed lines indicate hyperbolic curve fitting of mean cross-flow velocity and mean helicity density, respectively.

small-scale helical motion was maximized at a specific κ value. At κ = 0.125, *RMS* values of u_y were very low due to the absence of transverse migration of fluid. *RMS* values of each velocity component increased as κ increased. *RMS* values of u_z significantly increased due to the lateral migration in the z-direction as a result of the effects of the grooves, as shown in Fig. 12(c). However, *RMS* values of u_y showed a different distribution. Like *RMS* values of u_z, *RMS* values of u_y within the non-grooved area increased as κ increased. *RMS* values of u_y within the grooved area increased until κ reached 0.500 and decreased as κ increased to 0.875, as shown in Fig. 12(b). In other words, for κ values smaller than 0.500, *RMS* values of u_y within the grooved area were higher than those within the non-grooved area. In contrast, *RMS* values of u_y within the grooved area were lower than those within the non-grooved area for κ values higher than 0.500. These results indicate that y-velocity fluctuations were induced where the grooved area changed to a non-grooved area.

We also investigated helical flow patterns for groove intersection angles ranging from 1.0 to 4.0 degrees with dimensions of h_{ch} = 50 μm, w_{ch} = 300 μm, α = 1.0 and κ = 0.500.

Helicity density distribution and cross-flow velocity distribution of the cross-sectional area are illustrated in Fig. 13(a). Maximum helicity density was observed near the edge of the bas-relief grooves, and helicity density was concentrated between groove patterns. Mean helicity density and cross-flow velocity were computed numerically along the channel in a longitudinal direction for different δ values, and the results are

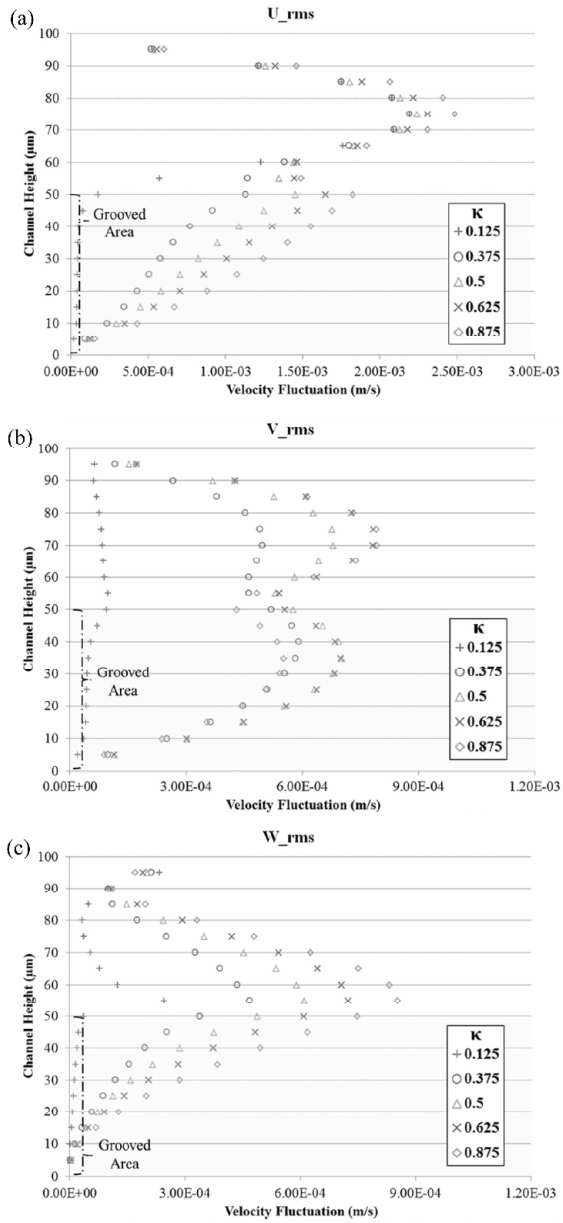

Fig. 12. Vertical profiles of the velocity fluctuation of (a) u_x; (b) u_y; (c) u_z for different values of κ.

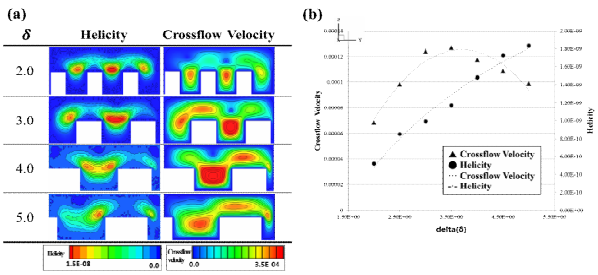

Fig. 13. (a) Helicity density distribution and cross-flow velocity distribution across the cross-sectional area orthogonal to the mainstream direction; (b) mean helicity density and mean cross-flow velocity plots for varying values of δ.

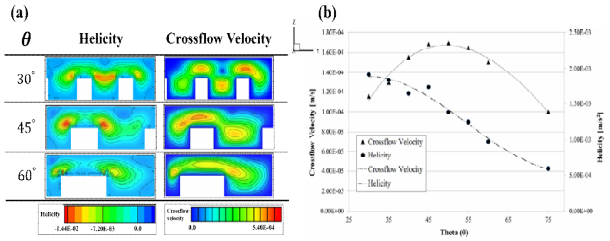

Fig. 14. (a) Helicity density distribution and cross-flow distribution across the cross-sectional area orthogonal to the mainstream direction; (b) mean helicity density and mean across-flow velocity plots for varying values of θ.

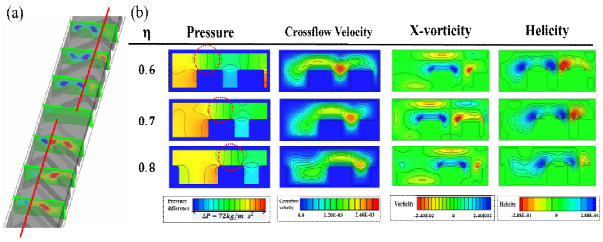

Fig. 15. (a) Helicity density distribution along the micro-mixer; (b) pressure contour, cross-flow velocity, x-vorticity and helicity density distribution across the cross-sectional area orthogonal to the mainstream direction for different values of η.

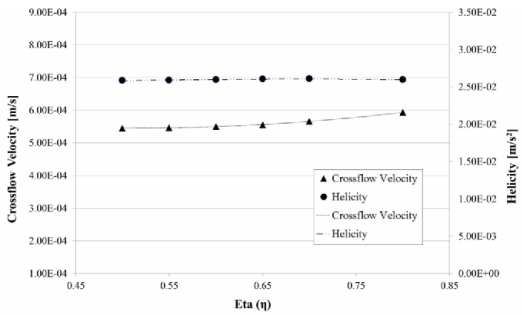

Fig. 16. Mean helicity density and mean cross-flow velocity plots for different values of η.

shown in Fig. 13(b). Mean helicity density increased for higher values of δ. Maximum cross-flow velocity was observed when δ was 4.0 and then decreased until an δ value of 5.0.

We also investigated helical flow patterns for groove intersection angles ranging from 30 to 75 degrees with dimensions h_{ch} = 50 μm, w_{ch} = 300 μm and κ = 0.625. Helicity density distribution and cross-flow velocity distribution of the cross-sectional area are illustrated in Fig. 14(a). Maximum helicity density was observed near the edge of the bas-relief grooves, and helicity density was spread over the channel. Mean helicity density and cross-flow velocity were computed numerically along the channel in a longitudinal direction for different θ values, and these results are shown in Fig. 14(b). A maximum mean helicity density was observed when θ was 30 degrees and decreased smoothly until θ reached 45 degrees. Mean helicity density decreased faster for θ values larger than 45 degrees. Finally, when θ was 60 degrees, the mean helicity density decreased to 50% of its maximum value. In contrast, the maximum cross-flow velocity was observed when θ was 45 degrees, and it decreased by 33% when θ was 30 degrees.

4.4 Staggered-herringbone micro-mixers (SHMs)

The SHM can be thought of as two SGM devices adjacent to each other. The herringbone groove asymmetric ratio, η, determines the relationship between the long grooves and the short grooves. Previous results confirmed that asymmetric vortices generated by the asymmetric herringbone shape resulted in more effective mixing than symmetric herringbone shape; specifically, chaotic advection was introduced by changeover of flow motion due to changes in the location of asymmetric grooves [25, 39]. The helical flow within each groove of an SHM adheres to the same mechanism of fluid mixing as in a SGM; thus, the base values of θ, α, κ were chosen based on the results of the SGM experiments.

We investigated secondary flow patterns for η values ranging from 0.5 (herringbone grooves installed symmetrically) to 0.8 with dimensions h_{ch} = 50 μm, w_{ch} = 300 μm, α = 1.0, θ = 45°, κ = 0.625. Fig. 15(a) shows that the helicity density value changed from positive to negative, which means that the rotation direction of helical motion was overturned by the bas-relief grooves. Cross-flow velocity within the channel was generated by the pressure difference between the groove and the protrusion along the channel direction; this behavior is similar to that of the SGM. We calculated the mean absolute helicity density ($H_{abs} = |H|$) and the mean cross-flow velocity for different values of η, as shown in Fig. 16. Unlike the results with different values of θ, α and κ, the mean absolute helicity density did not change notably with different values of η. This indicates that the flow patterns that produced helical motion do not have a significant effect on fluid flow with varying values of η.

The mean cross-flow velocity gradually increased as η increased. At η = 0.8, the mean cross-flow velocity was about 7% higher than that observed when η = 0.5. This means that η did not have a significant effect on the transverse migration of flow, in contrast to θ, α and κ. The pressure differences that drove fluid flow inside the micro-mixers did not change significantly as η changed, in contrast to the SGM results shown in Fig. 17. Furthermore, because the α, κ and θ of the grooved channel were the same as those of the SGM, the values of *x*- and *z*- vorticity induced by grooves and the protrusion were almost the same. Thus, the mean absolute helicity density and the mean cross-flow velocity did not vary significantly for different values of η. Therefore, η is not a major factor influencing helical motion. Helicity and crossflow velocity distributions alone cannot fully explain the chaotic advection effect.

RMS values of each velocity component are shown in Fig. 18. At the groove, the *RMS* values of u_x increased slightly as η increased. As the asymmetry of the herringbone groove in-

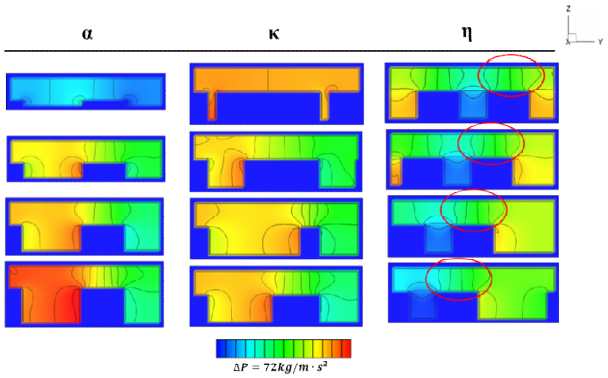

Fig. 17. Pressure contours across the cross-sectional area orthogonal to the mainstream direction for various values of α, κ and η.

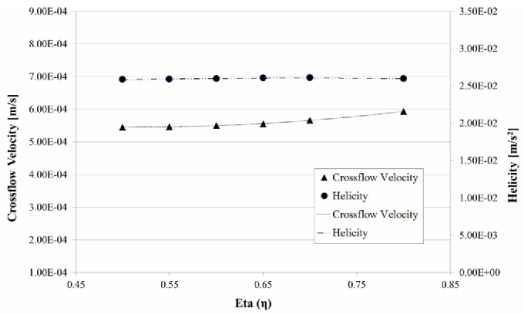

Fig. 18. Mean helicity density and mean cross-flow velocity plots for different values of η.

creased, *RMS* values of u_y increased through the whole channel, while those of u_z decreased. This indicates that the direction and amount of transverse migration in the fluid slightly shifted from the *y*-direction to the *z*-direction as η increased.

4.5 Bi-layered staggered-herringbone micro-mixers (BSHMs)

BSHM has patterned grooves not only on the bottom wall, but also on the upper wall of the channel. Research groups have used both conventional and novel methods to enhance the mixing efficiency of BSHMs and ensure that they provide better mixing than SHMs [29, 30]. However, staggered herringbone grooves were created symmetrically on both sides. Therefore, we investigated the helical motion of flow with asymmetric installation of grooves on both sides. We varied the bi-layered groove asymmetric ratio, γ, from 0 (herringbone grooves installed symmetrically) to 0.5 with dimensions h_{ch} = 50 μm, w_{ch} = 300 μm α = 1.0, κ = 0.500 and $\eta = 2/3$; this is the same herringbone groove *asymmetric* ratio used by Choudhary et al. [29]. When γ was 0, four transverse flow patterns were observed, and two small and two large vortices were generated, as shown in Fig. 19. Helicity density was distributed symmetrically on the upper and lower sides of the channel, with opposite signs.

As γ increased, pressure difference patterns significantly changed, resulting in a cross-flow velocity. Thus, the symmetry of both properties was disrupted, and the layer that divided

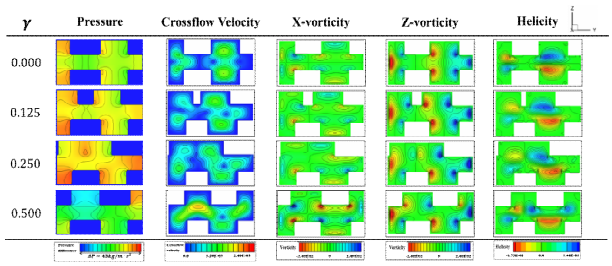

Fig. 19. Pressure contour, cross-flow velocity, x-, z-vorticity and helicity density distribution across the cross-sectional area orthogonal to the mainstream direction for different values of γ.

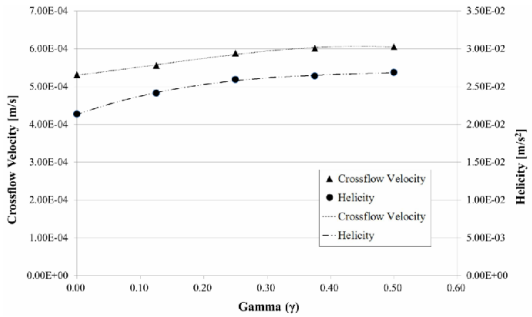

Fig. 20. Mean helicity density and mean cross-flow velocity plots for different values of γ.

the upper and the lower sides experienced stirring. This signifies that the lateral migration along the z-direction proceeded within the whole channel. As shown in Figs. 21(b) and (c), the *RMS* value of u_z increased as γ increased to 0.5. This result explains the increase in fluid migration along the *z*-direction. In contrast, the *RMS* value of u_y decreased within the non-grooved area as γ increased. This indicates that the direction and amount of transverse migration of the fluid shifted from the *y*-direction to the *z*-direction as the asymmetry of the bi-layered grooves increased. We calculated the mean absolute helicity density and the mean cross-flow velocity for different values of γ, and the results are shown in Fig. 20. Mean absolute helicity density increased gradually by about 23% as γ was varied from 0 to 0.5, while the mean cross-flow velocity increased gradually by about 14%. Asymmetric installation of grooves on both sides enhanced helical motion.

5. Conclusions

We performed hydrodynamic analyses to investigate the helical motion of the fluid flow of water with a low Reynolds number by varying several geometric parameters for SGM, SHM and BSHM mixers. Numerical simulations using D3Q19 lattice Boltzmann methods revealed that helical motion and transverse migration were maximized by changing the bas-relief groove designs and bi-layered asymmetric structures. We focused on five geometric parameters and performed geometric parameter analysis through simulation to determine the effect of each parameter on fluid flow. Oblique groove patterns played a significant role in generating the

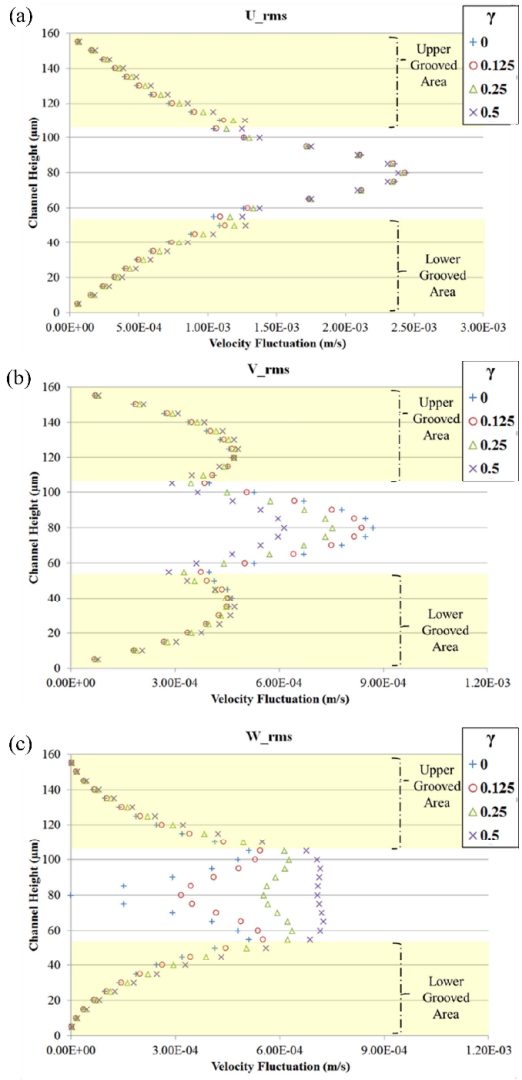

Fig. 21. Vertical profiles of the velocity fluctuation of (a) u_x; (b) u_y; (c) u_z for different values of γ.

helical flow inside the channel due to their ability to generate *x*- and *z*-vorticity. Groove height to channel height ratio, α, and groove width to groove pitch length ratio, κ, had the greatest effect on helical flow motion over grooved surfaces.

The herringbone groove asymmetric ratio, η, was also an important parameter related to chaotic advection. However, its influence on helicity density and cross-flow velocity was relatively small because it contributed to pressure differences in the cross-sectional area and generation of *x*- and *z*-vorticity along the protrusion. Asymmetry of the bi-layered grooves also enhanced helical motion and transverse migration of the fluid. Using velocity fluctuation analysis, we confirmed that asymmetry of the bi-layered grooves disrupted the layer structure between the upper and lower areas and induced fluid transportation. On the other hand, flow with a low Reynolds number was affected by the viscosity of fluid; thus, the geometric effects on the fluid mixing within the micro-channel vary for fluids of different viscosity.

Acknowledgement

This work was partially supported by the Mid-Career Researcher Programs (NRF-2015R1A2A1A15056182) and by the Advanced Research Center Program (NRF-2015R1A5 A1037668) through a National Research Foundation of Korea (NRF) grant funded by the Ministry of Science, ICT, and Future Planning (MSIP).

References

[1] D. F. Hayes, J. Allen, C. Compton, G. Gustavsen, D. G. B. Leonard, R. McCormack, L. Newcomer, K. Pothier, D. Ransohoff, R. L. Schilsky, E. Sigal, S. E. Taube and S. R. Tunis, Breaking a Vicious Cycle, *Sci. Transl. Med.,* 5 (196) (2013).

[2] M. Wendel, L. Bazhenova, R. Boshuizen, A. Kolatkar, M. Honnatti, E. H. Cho, D. Marrinucci, A. Sandhu, A. Perricone, P. Thistlethwaite, K. Bethel, J. Nieva, M. van den Heuvel and P. Kuhn, Fluid biopsy for circulating tumor cell identification in patients with early-and late-stage non-small cell lung cancer: glimpse into lung cancer biology, *Phys. Biol.*, 9 (1) (2012) 016005.

[3] D. C. Danila, M. Fleisher and H. I. Scher, Circulating Tumor Cells as Biomarkers in Prostate Cancer, *Clin Cancer Res.,* 17 (2011) 3903.

[4] J. M. Lang, B. P. Casavant and D. J. Beebe, Circulating Tumor Cells: Getting More from Less, *Sci. Transl. Med*., 4 **(**141) (2012).

[5] Z. Liu, F. Huang, J. Du, W. Shu, H. Feng, X. Xu and Y. Chen, Rapid isolation of cancer cells using microfluidic deterministic lateral displacement structure, *Biomicrofluidics*, 7 (1) (2013) 011801.

[6] J. Sun, C. Liu, M. Li, J. Wang, Y. Xianyu, G. Hu and X. Jiang, Size-based hydrodynamic rare tumor cell separation in curved microfluidic channels, *Biomicrofluidics,* 7 (1) (2013) 011802.

[7] M. Alshareef, N. Metrakos, E. J. Perez, F. Azer, F. Yang, X. Yang and G. Wang, Separation of tumor cells with dielectrophoresis-based microfluidic chip, *Biomicrofluidics*, 7 (1) (2013) 011803.

[8] R. Manzoor, S. Ul. Islam, W. S. Abbasi and S. Parveen, Variation of wake patterns and force coefficients of the flow past square bodies aligned inline, *Journal of Mechanical Science and Technology*, 30 (4) (2016) 1691.

[9] I. Cima, C. W. Yee, F. S. Iliescu, W. M. Phyo, K. H. Lim, C. Iliescu and M. H. Tan, Label-free isolation of circulating tumor cells in microfluidic devices: Current research and perspectives, *Biomicrofluidics*, 7 (1) (2013) 011810.

[10] A. Kumar and A. Srivastava, Nat Protoc, Cell separation using cryogel-based affinity chromatogra*phy, Nature Protocols*, 5 (11) (2010) 1737.

[11] S. Wang, K. Liu, J. Liu, Z. T.-F. Yu, X. Xu, L. Zhao, T. Lee, E. K. Lee, J. Reiss, Y.-K. Lee, L. W. K. Chung, J.

Huang, M. Rettig, D. Seligson, K. N. Duraiswamy, B. K.-F. Shen and H.-R. Tseng, Highly efficient capture of circulating tumor cells by using nanostructured silicon substrates with integrated chaotic miromixers, *Angew. Chem. Int. Ed.*, 50 (13) (2011) 3084.

[12] GS. L. Scott, C-H. Hsu, D. I. Tsukrov, M. Yu, D. T. Miyamoto, B. A. Waltman, S. M. Rothenberg, A. M. Shah, M. E. Smas, G. K. Korir, F. P. Floyd, Jr, A. J. Gilman, J. B. Lord, D. Winokur, S. Springer, D. Irimia, S. Nagrath, L. V. Sequist, R. J. Lee, K. J. Isselbacher, S. Maheswaran, D. A. Haber and M Toner, Isolation of circulating tumor cells using a microvortex-generating herringbone-chip, *Natl. Acad. Sci.*, 107 (43) (2010) 18392.

[13] C-Y. Lee, C-L. Chang, Y-N. Wang and L-M Fu, Microfluidic mixing : A review, *Int. J. Mol. Sci.*, 12 (5) (2011) 3263.

[14] A. Dodge, M-C. Jullien, Y-K. Lee, X. Niu, F. Okkels and P. Tabeling, An example of a chaotic micromixer: the cross-channel micromixer, *C. R. Physique,* 5 (2004) 557.

[15] M. Campisi, D. Accoto, F. Damiani and P. Darlo, A soft-lithographed chaotic electrokinetic micromixer for efficient chemical reactions in lab-on-chips, *J. Micro-Nano Mech.*, 5 (3-4) (2009) 69.

[16] Y. Wang, J. Zhe, B. T. F. Chung and P. Dutta, A rapid magnetic particle driven micromixer, *Microfluid Nanofluid*, 4 (5) (2008) 375.

[17] D. Ahmed, X. Mao, B. K. Juluri and T. J. Huang, A fast microfluidic mixer based on acoustically driven sidewall-trapped microbubbles, *Microfluid Nanofluid*, 7 (5) (2009) 727.

[18] T.-D. Luong, V.-N. Phan and N.-T. Nguyen, High-throughput micromixers based on acoustic streaming induced by surface acoustic wave, *Microfluid Nanofluid*, 10 (3) (2011) 619.

[19] R.-T. Tsai and C.-Y. Wu, An efficient micromixer based on multidirectional vortices due to baffles and channel curvature, *Biomicrofluidics*, 5 (1) (2011) 014103.

[20] F. Jiang, K. S. Drese, S. Hardt, M. Küpper and F. Schönfeld, Helical flows and chaotic mixing in curved miro channels, *AIChE J.,* 50 (9) (2004) 2297.

[21] C. K. Chung and T. R. Shih, Effect of geometry on fluid mixing of the rhombic micromixers, *Microfluid Nanofluid*, 4 (5) (2008) 419.

[22] S. Hardt, H. Pennemann and F. Schönfeld, Theoretical and experimental characterization of a low-Reynolds number split-and-recombine mixer, *Microfluid Nanofluid*, 2 (3) (2006) 237.

[23] X. Chen and X. Wang, Optimized modular design and experiment for staggered herringbone chaotic micromixer, *International Journal of Chemical Reactor Engineering ISSN* (2015) 7542-6580.

[24] A. D. Stroock, S. K. W. Dertinger, A. Ajdari, I. Mezić, H. A. Stone and G. M. Whitesides, Chaotic mixer for microchannels, *Science*, 295 (5555) (2002) 647.

[25] F. Schönfeld and S. Hardt, Simulation of helical flows in microchannels, *AIChE J.*, 50 (4) (2004) 771.

[26] C. Li and T. Chen, Simulation and optimization of chaotic micromixer using lattice Boltzmann method, *Sens. Actuators B.*, 106 (2) (2005) 871.

[27] N. S. Lynn and D. .S. Dandy, Geometrical optimization of helical flow in grooved micromixers, *Lab on a Chip*, 7 (5) (2007) 580.

[28] T. P. Forbes and J. G. Kralj, Engineering and analysis surface interactions in a microfluidic herringbone mixromixer, *Lap Chip,* 12 (2012) 2634-2637.

[29] H. Wang, P. Iovenitti, E. Harvey and S. Masood, Passive mixing in microchannels by applying geometric variations, *Proc. SPIE, Microfluidics, BioMEMS, and Medical Microsystems*, 4982 (2003) 282.

[30] H. Wang, P. Iovenitti, E. Harvey and S. Masood, Numerical investigation of mixing in microchannels with patterned grooves, *J. Micromech. Microeng.*, 13 (2003) 801.

[31] F. M. Mastrangelo, F. Pennella, F. Consolo, M. Rasponi, A. Redaelli, F. M. Montevecchi and U. Morbiducci, Micromixing and microchannel design: vortex shape and entropy, *2nd Micro and Nano Flows Conference* (2009).

[32] P. E. Geyer, N. R. Rosaguti, D. F. Fletcher and B. S. Haynes, Thermohydraulics of square-section microchannels following a serpentine path, *Microfluid Nanofluid*, 2 (2006) 195.

[33] R. Choudhary, T. Bhakat, R. K. Singh, A. Ghubade, S. Mandal, A. Ghosh, A. Rammohan, A. Sharma and S. Bhattacharya, Bilayer staggered herringbone micro-mixers with symmetric and asymmetric geometries, *Microfluid Nanofluid*, 10 (2) (2011) 271.

[34] D. Lin, F. He, Y. Liao, J. Lin, C. Liu, J. Song and Y. Cheng, Three-dimensional staggered herringbone mixer fabricated by femtosecond laser direct writing, *Journal of Optics,* 15 (2) (2013) 025601.

[35] Y. H. Qian, D. d'Humières and P Lallemand, Lattic BGK models for Navier-Stokes equation, *Europhys. Lett.*, 17 (6) (1992) 479-484.

[36] S. Succi, *The Lattice Boltzmann equation for fluid dynamics and beyond*, Oxford University Press (2001).

[37] H. K. Moffatt, The degree of knottedness of tangled vortex lines, *Journal of Fluid Mech.*, 25 (1) (1969) 117-129.

[38] J. C. R. Hunt and F. Hussain, A note on velocity, vorticity and helicity of inviscid fluid elements, *Journal of Fluid Mech*, 229 (1991) 569-587.

[39] N.-T. Nguyen and Z. Wu, Micromixers-a review, *Journal Mircomech Microeng*, 15 (2005) R1-R16.

Joon Sang Lee is an Associate Professor of School of Department of Mechanical Engineering, Yonsei University, Seoul, Republic of Korea. He received his doctor degree in Mecha- nical Engineering from Iowa State University. His research interests is mainly on computational fluid dynamics, including biomechanics and hemodynamics and multi-scale fluid dynamics.